Implementation of a Semi-Implicit Orbit-Averaged Gyrokinetic Particle Code

BRUCE I. COHEN AND TIMOTHY J. WILLIAMS

Lawrence Livermore National Laboratory, University of California, Livermore, California 94550

[Published as J. Comput. Phys. **107**, 282 (1993).]

A semi-implicit orbit-averaged time-integration algorithm has been successfully implemented in a gyrokinetic particle simulation code for the study of self-consistent phenomena in a strongly magnetized plasma. The semi-implicit aspect of the integration scheme relaxes the timestep constraints required to insure numerical stability. The orbit averaging is useful in reducing statistical noise and relaxes the statistical constraints for kinetic simulation. For appropriate applications, the semi-implicit orbit-averaged algorithm should be more efficient than are traditional particle-in-cell plasma simulation algorithms with explicit time-integration schemes. Both a linear numerical dispersion analysis and illustrative simulation examples are presented.

1. Introduction

Kinetic phenomena in laboratory and space plasmas span many orders of magnitude making direct numerical solution of the fundamental equations computationally intensive (if not hopeless) in many circumstances [1]. This paper presents first results from the implementation of a semi-implicit orbit-averaged particle simulation algorithm that addresses the disparate timescale problem in the simulation of kinetic plasma phenomena. This study continues our earlier work [2] in which model algorithms and linear numerical dispersion analyses were presented that introduced both semi-implicit and semi-implicit orbit-averaged algorithms for self-

consistent particle simulation of plasmas. Here we report our experience implementing a semi-implicit orbit-averaged time-integration scheme in an electrostatic gyrokinetic particle simulation algorithm with kinetic electrons and ions [3]. We have determined that modifications to the basic algorithm presented in [2] are required to suppress a slowly growing numerical error. A linear dispersion analysis of the revised algorithm and results from a few illustrative simulation examples are presented. The analysis and examples demonstrate that the semi-implicit orbit-averaged algorithm relaxes constraints on both the timestep required for stability of the highest frequency waves in the model and the statistical resolution. The combination of implicit time integration and orbit averaging leads to a more efficient self-consistent particle code for appropriate physics applications. However, the improvement in efficiency is sensitive to the details of the specific physics application.

The motivation for this work, that reported in [2], and the earlier work on direct implicit particle simulation [4] and orbit averaging [5,6] is the desire to study time-dependent, collective kinetic phenomena in a plasma having a wide range of timescales so that the computational problem is quite stiff [1]. The class of phenomena motivating our specific choice of a gyrokinetic particle code as a testbed for a semi-implicit orbit-averaged time-integration scheme is low-frequency microturbulence in magnetically confined plasmas, e.g., drift-wave instabilities.

The gyrokinetic algorithm analytically removes the cyclotron timescale by a formal time averaging [3], while retaining the effects of the finite Larmor radius on the interaction of the particles with the self-consistent fields for frequencies much less than the cyclotron frequency. This assumption is compatible with a large class of drift-wave instabilities and low-frequency magnetohydrodynamic (MHD) and resistive modes that are believed to contribute significantly to the turbulent transport of energy and particles observed in tokamak experiments. Even with the use of the gyrokinetic formalism, the kinetic simulation of drift-wave instabilities in tokamaks remains a stiff problem. The timescales of electrons transiting across a drift wave following the equilibrium magnetic field lines are many orders of magnitude shorter than the periods of the drift waves producing transport. Furthermore, an explicit time integration of the electrostatic

equations with kinetic electrons is subject to a timestep constraint set by the highest frequency normal mode, $\omega_h \Delta t < 1$ where $\omega_h \equiv (k_\parallel/k_\perp)(m_i/m_e)^{1/2}\, \Omega_i$ where $\Omega_i = eB_0/m_i c$ is the ion cyclotron frequency, m_i/m_e is the mass ratio, and $k_\parallel/k_\perp$ is the ratio of the parallel and perpendicular wavenumbers with respect to the equilibrium magnetic field; ω_h is typically much larger than the drift-wave frequencies. As explained in [2], the semi-implicit orbit-averaged algorithm seeks to relax the timestep constraint set by ω_h and reduce the statistical constraint on the electrons without forfeiting an accurate calculation of their trajectories.

The paper is organized as follows. In Sec. 2 we describe our implementation of the semi-implicit orbit-averaged gyrokinetic algorithm introduced in [2]. The linear dispersion analysis of this integration scheme in [2] indicated that exponentially growing modes can be stabilized at large timestep. However, trial simulations reveal numerically unstable zero-frequency modes that grow algebraically in time. A variant of this algorithm is then introduced, and a linear dispersion analysis shows that the stability boundary for exponentially growing modes is extended to a timestep that is significantly larger than the maximal stable timestep for the explicit time-integration scheme used in [3]. The effects of spatial filtering and interpolation onto a spatial grid modify the linear dispersion analysis. Simulation results for a few test cases using the revised algorithm are presented in Sec. 3. A simulation of an ion-temperature-gradient instability [7] is used as a convenient test problem with which to compare the simulation results of our algorithm and those from an explicit integration scheme. These results are in substantial agreement with those published in [7] for small timestep. In this example, finite-amplitude effects limit how large a timestep may be used and limit the usefulness and applicability of orbit averaging. Nevertheless, it is demonstrated that orbit averaging can lead to a substantial reduction of the number of particles. Additional simulations for a stable ion-temperature-gradient mode are reported that illustrate the stability properties of the revised semi-implicit orbit-averaged algorithm and demonstrate both its noise-reduction characteristics and improved computational efficiency. Some concluding remarks are given in Sec. 4.

2. Semi-Implicit Orbit-Averaged Algorithms

In this section we shall begin by reviewing the algorithm introduced in [2] and describing both the results of a linear stability analysis and the failure of this algorithm because of a zero-frequency error that grows linearly in time. A revised algorithm is introduced that is designed to remove the secularly growing error. A linear dispersion analysis for the highest-frequency, cold-plasma normal mode is then presented. Some comments on how spatial grid effects and spatial filtering alter the linear dispersion relation are also given here.

2.1 First Algorithm

The first semi-implicit orbit-averaged algorithm was introduced in [2] for gyrokinetic simulation. The electrons were modeled as a drift-kinetic species (zero Larmor radius), while Larmor radius effects were retained in the gyrokinetic limit for the ions. Equations (17-21) in [2] describe the scheme in detail. The basic algorithm is composed of the following elements. In an electrostatic model, the electrons are advanced with a small timestep Δt_e from $N\Delta t_i$ to $(N+1)\Delta t_i$ using the electric field $\mathbf{E}_N = -\nabla f_N$ in a static magnetic field. The electron charge and current densities n^e and $\mathbf{J}^e$ are accumulated on the spatial grid at each timestep from the particle data $\{\mathbf{x}^e, \mathbf{v}^e\}$ and then time-averaged to form $\langle n^e \rangle$ and $\langle \mathbf{J}^e \rangle_{N+1/2}$. The ion gyro-centers are then advanced in a predictor step from $N\Delta t_i$ to $(N+1)\Delta t_i$ using the appropriately gyro-averaged electric field [3]. A predicted gyro-averaged ion number density $\bar{n}^{\,i}$ is collected from the ion positions $\left\{\tilde{\mathbf{x}}^i_{N+1}\right\}$ displaced by their Larmor radii. The self-consistent electric potential $\tilde{f}_{N+1}$ is determined by the solution of the semi-implicit gyrokinetic Poisson equation,

$$-\left(\nabla^2+\frac{w_{pi}^2}{\Omega_i^2}\nabla_\perp^2 g\right)\left(\tilde{f}_{N+1}-f_N\right)=4pe\left(\bar{n}_{N+1}^i-\bar{n}_N^i\right)-4p\Delta t_i\nabla\cdot\left\langle \mathbf{J}^e\right\rangle_{N+1/2}$$
$$+C_0\nabla_\parallel\left[\bar{w}_{pe}^2\Delta t_i^2\nabla_\parallel\left(\tilde{f}_{N+1}-f_N\right)\right] \qquad (1)$$

where $\bar{w}_{pe}^2\equiv 4p(e^2/m_e)\left\langle n^e\right\rangle_{N+1/2}\approx 4pn_0e^2/m_e$, $w_{pi}^2=4pn_0e^2/m_i$, $g=b^{-1}[1-I_0\exp(-b)]$ in **k** space, $b\equiv k_\perp^2\bar{r}_i^2$, $\bar{r}_i=(T_i/m_i)^{1/2}/\Omega_i$ is the Larmor radius Ω_i ,is the ion cyclotron frequency, and C_0 is a control parameter for the implicitness. Recall that the gyrokinetic ordering [2,3] assumes that the density perturbations considered, although finite, are small in amplitude, and the inhomogeneities of the unperturbed plasma are weak. In consequence, the plasma parameters appearing in the ion polarization and the semi-implicit electron susceptibility are homogeneous and constant. The ions are then advanced in a corrector step from $N\Delta t_i$ to $(N+1)\Delta t_i$ using $\tilde{\mathbf{E}}_{N+1}=-\nabla\tilde{f}_{N+1}$ and $\mathbf{E}_N$. The corrected value of $\bar{n}_{N+1}^i$ is then calculated and used in Eq.(1) to obtain f_{N+1}. The timestep advance to $(N+1)\Delta t_i$ is completed by using an electric field $\mathbf{E}=\mathbf{E}_N+2C_0(\mathbf{E}_{N+1}-\mathbf{E}_N)$, where $\mathbf{E}_{N+1}=-\nabla f_{N+1}$* to correct the advance of the electrons from $N\Delta t_i$ to $(N+1)\Delta t_i$.

A linear stability analysis was performed in [2] to obtain the following model dispersion relation in the limit of a cold, non-drifting plasma and with spatial grid and interpolation effects neglected:

$$\left(1+C_0w_h^2\Delta t_i^2\right)(l-1)^2+w_h^2\Delta t_i^2\left[(2C_0+1/2)(l-1)+1\right]=0 \qquad (2)$$

where $l=\exp(-iw\Delta t_i)$, $w_h^2\equiv(k_\parallel^2/k_\perp^2)(m_i/m_e)\Omega_i^2$, and $k_\parallel^2\ll k_\perp^2$. The parallel and perpendicular subscripts indicate the orientation of the wavenumber components relative to the magnetic field. For $C_0>1/4$, there are damped solutions ($|l|<1$) of Eq.(2): for $w_h^2\Delta t_i^2\gg 1$, $l=\{1-1/(2C_0),-1+O(1/w_h^2\Delta t_i^2)\}$; for $w_h^2\Delta t_i^2\ll 1$ there are damped solutions with $\mathrm{Re}(w)\approx\pm w_h$. In Fig. 1 we plot the modulus of the amplification factor for the two roots of Eq.(2).

Thus, for C_0>1/4 there are no exponentially growing modes. However, perturbations growing with a power-law dependence on time are not excluded.

In our unsuccessful attempts to implement this algorithm, we discovered several difficulties. The first difficulty was that Eq.(1) treats the ion and electron source terms in Eq.(1) on an unequal footing. The electron current was accumulated and then its divergence calculated on the grid, while an ion charge density was calculated directly. To put the electrons and ions on a more equal footing with respect to finite-differencing, which might be important in resolving small deviations from quasi-neutrality, we made the replacement $4pe\left(\bar{n}^i_{N+1} - \bar{n}^i_N\right) = -4p\nabla\cdot\tilde{\mathbf{J}}^i_{N+1}$ in Eq.(1), where $\tilde{\mathbf{J}}^i_{N+1}$ is the gyro-averaged ion current density at $(N+1)\Delta t_i$ on the ion predictor step and is determined from $\{\tilde{\mathbf{x}},\tilde{\mathbf{v}}\}^i_{N+1}$. On the ion corrector step, $\tilde{\mathbf{J}}^i_{N+1}$ was accumulated from $\{\mathbf{x},\mathbf{v}\}^i_{N+1}$. This modification leaves the dispersion relation derived in Eq.(2) unchanged. However, a second difficulty remains and manifests itself in zero-frequency errors in the potential and perturbed plasma displacements that grow approximately linearly in time (Fig.2). Although we were able to verify the algorithm's stability properties with respect to exponentially growing modes for large values of $w_h^2\Delta t_i^2$ when C_0>1/4, or instability when C_0<1/4, the presence of the secularly growing error frustrated successful simulation of physical instabilities like the ion-temperature-gradient (ITG) mode [7]. We believe that the secularly growing errors derive from grid errors and statistical effects in the ion and electron source terms on the right side of Eq.(1) that linearly accrue in f at each timestep on account of the time integration of Eq.(1). In **k**-space, Eq.(1) has the form $f_{N+1}=f_N+L_{\mathbf{k}}S_{\mathbf{k}}$, where $L_{\mathbf{k}}$ is a linear operator and $S_{\mathbf{k}}$ is a source. By replacing Eq.(1), with a semi-implicit Poisson equation that uses the ion charge density and the orbit-averaged electron charge density, we were able to remove the secularly growing error.

2.2 Revised Algorithm

We have revised our semi-implicit orbit-averaged algorithm to remove the secularly growing errors as follows. The interleaving of the ion and electron advances is diagrammed in

Fig. 3. The electrons are advanced in a predictor step from $(N+1/2)\Delta t_i$ to $(N+3/2)\Delta t_i$ using a small timestep Δt_e and the electric field $\mathbf{E}_N$. The orbit-averaged electron number density $\langle n^e \rangle_{N+1}$ is accumulated by averaging the electron densities calculated at each electron timestep over this time interval. The ions are advanced in a predictor step from $N\Delta t_i$ to $(N+1)\Delta t_i$ using the larger timestep Δt_i and the electric field $\mathbf{E}_{N+1}$ in a conventional way [2,3]. A gyroaveraged ion number density $\bar{n}^i_{N+1}$ is accumulated at $(N+1)\Delta t_i$. The revised semi-implicit gyrokinetic Poisson equation is solved following the ion advance,

$$-\left(\nabla^2 + \frac{w_{pi}^2}{\Omega_i^2}\nabla_\perp^2\right)\tilde{f}_{N+1} = 4pe\left(\bar{n}^i_{N+1} - \left\langle n^e \right\rangle_{N+1}\right) + \nabla\cdot\left(C_0 \mathbf{?}_e \cdot \nabla\left(\tilde{f}_{N+1} - f_N\right)\right) \tag{3}$$

where c^e is the semi-implicit susceptibility tensor and is defined in the following.

The susceptibility is derived by relating the linearized drift-kinetic electron response to the electric field. For a slab configuration with $\mathbf{B} = B_0\hat{\mathbf{z}} + B_y\hat{\mathbf{y}}$, $|B_0/B_y|<<1$, and equilibrium density gradient in the x direction, both the parallel electron response and the perpendicular $\mathbf{E}\times\mathbf{B}$ drift lead to charge density perturbations. Hence, Eq.(3) in the drift-kinetic limit for the electrons becomes

$$\begin{aligned}-\left(\nabla^2 + \frac{w_{pi}^2}{\Omega_i^2}\nabla_\perp^2\right)\tilde{f}_{N+1} - C_0\left(\nabla_\parallel w_{pe}^2\Delta t_i^2\nabla_\parallel + 2\frac{w_{pe}^2\Delta t_i^2}{\Omega_e\Delta t_i}\frac{1}{L_n}\frac{\partial}{\partial y}\right)\left(\tilde{f}_{N+1} - f_N\right) \\ = 4pe\left(\bar{n}^i_{N+1} - \left\langle n^e \right\rangle_{N+1}\right)\end{aligned} \tag{4}$$

The two semi-implicit terms contribute to relaxing the $w_h\Delta t_i$ stability constraint and to compensating for the lack of centering in the electron charge density response which impacts the temporal accuracy. The validity criterion for linearization leading to the semi-implicit susceptibility is obtained from the straightforward extension of the corresponding condition derived for the direct implicit method [4,8] to a magnetized plasma, $\left|k_\parallel^2 (e/m_e) f \Delta t_i^2\right| > 1$. This

condition is a statement that the parallel displacement produced by the acceleration due to the electric field during a timestep must be smaller than a relevant wavelength to be resolved. This is a timestep constraint on the integration of the electron trajectory that must be satisfied whether or not the integration scheme is implicit and does not limit the nonlinearity of the electron response.

The ions are advanced in a corrector step from $N\Delta t_i$ to $(N+1)\,\Delta t_i$ using $\tilde{\mathbf{E}}_{N+1} = -\nabla \tilde{f}_{N+1}$ and $\mathbf{E}_N$ as described in [2,3]. The corrected ion positions $\left\{\mathbf{x}^{\,i}_{N+1}\right\}$ are used to accumulate $\bar{n}^{\,i}_{N+1}$, and Eq.(4) is solved to determine the corrected value of f_{N+1} from which $\mathbf{E}_{N+1} = -\nabla f_{N+1}$. Next the electron trajectories from $(N+1/2)\Delta t_i$ to $(N+3/2)\Delta t_i$ are recomputed in a corrector step again using a small timestep Δt_e. The electrons are advanced with an electric field $\mathbf{E} = C_0 \tilde{\mathbf{E}}_{N+1} + (1 - C_0)\mathbf{E}_N$ for this corrector step. This completes the computational cycle.

The highest frequency normal mode supported by these equations in a cold uniform plasma has frequency w_h defined in Sec. 1. The linear dispersion relation including Δt effects is obtained straightforwardly using the methods of Refs. [1,2,5,6]. For the w_h mode, the parallel electron response dominates the right side of Eq.(4); and $(w_{pi}^2/\Omega_i^2)\nabla_\perp^2 g \to (w_{pi}^2/\Omega_i^2)\nabla_\perp^2 >> \nabla^2$ for a cold, high-density plasma. For a small-amplitude, linear charge density perturbation, the right side of Eq.(4) becomes

$$\begin{aligned} 4pe\left(\bar{n}^{\,i}_{N+1} - \left\langle n^e \right\rangle_{N+1}\right) &\approx 4pe\nabla_\parallel \left[n_0 \sum_{j=0}^{N_*} x^e_{\parallel j} \,/\left(N_* + 1\right)\right] \\ &= 4pe\nabla_\parallel \left[n_0 \left(x^e_{\parallel N+1/2} + \frac{\Delta t_i}{2} v^e_{\parallel N+1/2} + \left(\frac{-e}{m_e}\right)\frac{\Delta t_i^2}{6} E_{\parallel N} \right)\right] \end{aligned} \tag{5}$$

where $N_* = \Delta t_i/\Delta t_e$ (we assume that $N_* >> 1$). Note that Eq.(5) corrects a typographical error in Eq.(7) of [6].

The linearized electron trajectory can be reduced to

$$x^e_{\|N+3/2} - x^e_{\|N+1/2} = \frac{\Delta t_i}{2}\left(v^e_{\|N+1/2} + v^e_{\|N+3/2}\right) \tag{6a}$$

$$v^e_{\|N+3/2} - v^e_{\|N+1/2} = -\frac{e}{m_e}\Delta t_i E^*_{\|} \tag{6b}$$

where $\mathbf{E}^*=\mathbf{E}_N$ on the predictor advance and $\mathbf{E}^*=C_0\mathbf{E}_{N+1}+(1-C_0)\mathbf{E}_N$ on the corrector advance; f_{N+1} is related by Eq.(4) and (5) to $x^e_{\|N+1/2}$, $x^e_{\|N+1/2}$, and f_N.Using the corrector version of Eqs.(6a) and (6b), we can relate the linearized values of $x^e_{\|}$ and $v^e_{\|}$ directly to $E_{\|N}$ and $E_{\|N+1}$. We then introduce the amplification factor l=exp(-$iw\,\Delta t_i$) and Fourier transform the spatial dependence to obtain

$$\tilde{x}^e = -\frac{\Delta t_i}{2}\frac{l^{1/2}(l+1)}{(l-1)^2}\left[C_0 + \frac{(1-C_0)}{l}\right]ik_{\|}\tilde{f} \tag{7a}$$

$$\tilde{v}^e = -\Delta t_i \frac{e}{m_e}\frac{l^{1/2}}{(l-1)}\left[C_0 + \frac{(1-C_0)}{l}\right]ik_{\|}\tilde{f} \tag{7b}$$

where $\tilde{x}^e$, $\tilde{v}^e$, and $\tilde{f}$ are Fourier amplitudes. Equations (4) and (5) are also Fourier analyzed to remove the spatial dependence, and we substitute $\tilde{E}_{\|} = -ik_{\|}\tilde{f}$, and $\tilde{x}^e$ and $\tilde{v}^e$ from Eqs.(7a) and (7b) to obtain the dispersion relation

$$l\,(l-1)^2 + a(l^2 + 4l + 1)(C_0 l + 1 - C_0) = 0 \tag{8}$$

where $a \equiv w_h^2\Delta t_i^2/6$.

There are three roots of Eq.(8) in general. For a>>1, there is one root l=(C_0-1)/C_0 that is stable for C_0≥1/2 and two unstable roots $l = -2 \pm \sqrt{3}$. For C_0=1 there is one stable root λ=0 and two additional roots that are stable if $\alpha \le 2$, *i.e.*, $w_h^2\Delta t_i^2 \le 12$. The general solution of Eq.(8) indicates that there is at least one unstable root for C_0<1 or $w_h^2\Delta t_i^2 > 12$. As C_0 is increased above

C_0=1, the instability threshold on the timestep decreases below $w_h^2\Delta t_i^2 = 12$. Sample solutions for $|l|$ as a function of a are plotted in Fig. 4. We conclude that the revised semi-implicit orbit-averaged algorithm relaxes the timestep constraint from $w_h^2\Delta t_i^2 \le O(1)$ to $w_h^2\Delta t_i^2 \le 12$. We note that in contrast to the direct-implicit algorithm [4], wherein the timestep set by the stability of the highest frequency mode is completely relaxed, the timestep constraint for this semi-implicit orbit-averaged algorithm is only partially relaxed. Of course, there are residual timestep constraints on any algorithm set by accuracy considerations in calculating the particle trajectories and the dielectric response [8], *e.g.*, $\mathbf{k}\cdot\mathbf{v}\Delta t<1$, so that an arbitrarily large timestep could never be used in practice. In Sections 3 and 4, we will describe how the $w_h^2\Delta t_i^2 \le 12$ constraint for the revised algorithm must compete with other timestep constraints that are sensitive to the specific physics application.

Our implementation of the semi-implicit orbit-averaged algorithm includes spatial filtering and spatial grid effects arising from the interpolations of the electric field force from the grid to the particles and the electron charge density from the particles to the grid. These alter the algorithm and the linear dispersion analysis in the same fashion as for the direct-implicit method [8,9]. The spatial smoothing factors, *e.g.*, a **k**-space filter like $\exp(-k^2a^2)$, and the interpolation factors that arise in $\bar{n}_{N+1}^i - \left\langle n^e \right\rangle_{N+1}$ on the right side of Eqs.(3) and (4) should be matched by the same factors in the semi-implicit susceptibility. This is straightforward and we refer to [9] for explicit formulae. The dominant effect is a reduction of the effective value of w_h^2 as $(k\Delta x/2)^2$ or k^2a^2 increases. As a consequence, the instability threshold on $w_h^2\Delta t_i^2$ becomes wavenumber dependent. Of course, thermal effects introduce additional dispersion; but this is physical. The Gaussian **k**-space filter can be suppressed by setting the smoothing factor a=0. There is nothing in the dispersion analysis to indicate that this cannot be done, but we have not tried it. Having a tunable spatial filter has been useful in our experience with other particle codes, and we will make use of it here.

Before concluding this section. We comment on accuracy considerations associated with the semi-implicit susceptibility. A criterion for whether low-frequency and long wavelength

modes of physical interest are being distorted can be derived from linear theory. The criterion derives from constraining the implicit susceptibility to be smaller than the linear electron susceptibility for the physical modes of interest.. For example, consider the linear electron susceptibility for adiabatic electrons, $c_e = 1/k^2 l_e^2$. The semi-implicit susceptibility produces a small modification if $C_0 k_\parallel^2 w_{pe}^2 \Delta t_i^2 < 1/l^2$, which is equivalent to $C_0 k_\parallel^2 v_e^2 \Delta t_i^2 < 1$ and similar to the stricter *stability* condition Eq.(41) in Ref.[6] involving the *largest* wavenumber retained. Because the modes of interest must satisfy $k_\parallel^2 \Delta x_\parallel^2 << 1$ for good resolution, this constraint does not preclude $\Delta t_e << \Delta t_i$. With a sufficiently small Δt_i, the longest, most important parallel wavelength will suffer an acceptably small distortion of the dielectric response because of the semi-implicit susceptibility.

3. Simulation Test Cases

The performance of the two-dimensional implementation of the revised semi-implicit orbit-averaged algorithm has been assessed in two types of test cases so far. The first test case was the unstable ITG mode investigated earlier in [7]. The second set of test cases was for a plasma that was stable to the ITG mode.

3.1 Ion-Temperature-Gradient Instability

In Figs. 5, 6, and 7, we show results from gyrokinetic simulations of an h_i=4 ITG instability, where $h_i \equiv (d \ln T_i/dx)/.(d \ln n_i/dx)$. Simulation results from an explicit, electron subcycled gyrokinetic code are presented in Fig. 5. The semi-implicit orbit-averaged algorithm was used to produce the results shown in Figs. 6 and 7. With electron subcycling [10], Poisson's equation and the electron equations of motion are solved together at each electron timestep Δt_e. The ions are advanced using a time-averaged electric field and a larger timestep that is an integer multiple of the electron timestep. The subcycling choreography and the stability

properties differ slightly depending on whether the ratio of the ion timestep to the electron timestep is odd or even; odd is preferred [10]. The value of the subcycling parameter was $N_* = \Delta t_i / \Delta t_e = 3$ for the simulation results shown in Figs. 5, 6, and 7. Because the ion gyrokinetic particle advance involves a much more complicated calculation than the electron drift-kinetic advance (the ion calculation is ~5 times more time consuming), there is a great benefit in computational efficiency from electron subcycling if it is compatible with accuracy and stability considerations.

A 16×16 grid was employed in all of the ITG test cases, $T_e = T_i$, $B_y/B_0 = 0.01$, no magnetic shear, and $\Delta x = \overline{r}_i$, where $\overline{r}_i = \left(T_i / m_i\right)^{1/2} / \Omega_i$ is the thermal ion Larmor radius. In addition, Lee's multiscale treatment of the ion temperature and density gradients was used [3]. There were 64 electrons and ions per cell used in the simulations shown in Figs. 5 and 6. There were 32 electrons and 64 ions per cell used in the orbit-averaged simulations whose results are displayed in Fig. 7. From linear theory, the complex frequency for the $(k_x,k_y)=(1,-1)$ (in units of $2\pi/L$) mode is $w/\Omega_i = 0.007 + 0.005i$ [7]. The unit charge per electron was twice that of the ions for the case with half as many electrons and ions. Further significant reduction of the number of orbit-averaged electrons relative to the number of ions did not lead to results with acceptable accuracy for the $h_i=4$ test case.

We note that there is reasonably good agreement between the simulation results shown in Figs. 5, 6, and 7. There is a significant degree of nonlinearity in the $h_i=4$ test case which influences the observed results and the best choice of simulation parameters. The mode frequency observed is significantly shifted by nonlinear effects from its linear value [7], and the maximum ion and electron velocities (derived from the **E**×**B** velocity) are large enough to limit the choice of timesteps. In fact, we noticed that there was sometimes a tendency for a strongly peaked potential structure to form, which was accompanied by a strong velocity vortex for both species. Once a strong velocity vortex formed, smaller timesteps were needed in both the explicit and semi-implicit simulations to insure that $v\Delta t < \Delta x$ for both species. To the extent that finite-amplitude effects narrow the disparity between the electron and ion velocities, so that the

ions are not much slower than the electrons, the improvement in efficiency to be gained from subcycling and orbit averaging diminishes. This unstable h_i=4 example establishes that the revised semi-implicit algorithm can obtain results that are in satisfactory agreement with those of a published benchmark, but no improvement in computational efficiency was achieved in this particular case because of finite-amplitude effects.

3.2 Simulation of a Warm, Quiescent, Nonuniform Plasma

The second test case set confirms some of the stability characteristics of the revised semi-implicit algorithm and demonstrates that a gain in computational efficiency can be obtained. In Fig. 8 we present simulation results for $|ef/T_e|$ for the $(k_x,k_y)=(1,-1)$ mode as a function of time from three simulations with h_i=1, $T_e=T_i$, $\overline{r}_i = \Delta x$, 16×16 grid, a smoothing factor $\exp(-k^2a^2)$ with a=1, and different choices of C_0, N_*, and $w_h\Delta t_i$. In all three simulations there were 256 ions and 64 electrons per cell. In Fig. 8a, C_0=1.04, N_*=16, and $w_h\Delta t_i$ =1.86; and the simulation is numerically stable. The simulation results in Fig. 8b reveal a numerical instability for C_0=0.5, N_*=16, and $w_h\Delta t_i$ =1.86; and in Fig. 8c for C_0=1.04, N_*=64, and $w_h\Delta t_i$ =7.4. These results are consistent with the stability boundaries determined in Section 2.2.

We show results from simulations with no gradients in Fig. 9, $T_e=T_i$, $\overline{r}_i = \Delta x$, 16×16 grid, 256 ions per cell, smoothing factor a=1.7, and various choices for N_* and the number of electrons per cell. These simulations of thermal noise are intended to show the influence of orbit averaging on important observables, such as the electric potential mode amplitudes and the ion thermal flux, and to address the questions of whether the orbit averaging reduces the noise and allows a reduction of the number of electrons. The results from one frame to the next should *not* be identical. We present results for $|ef/T_e|$ for the $(k_x,k_y)=(1,-1)$ mode and the spatially averaged ion thermal flux in the x direction normalized to the mean ion thermal energy times the sound speed as functions of time in Fig. 9. The deviations of the thermal flux from zero are due purely to statistical noise and thermal fluctuations. Both ions and electrons contribute to the statistical

noise. The orbit averaging of the electrons can reduce only the electron contribution to the noise. For equal numbers of ions and electrons, increasing N_* reduces the electron contribution to the statistical noise; but the ion contribution to the noise should persist (Fig. 9). With $N_*>>1$, we were able to reduce the number of electrons significantly, *e.g.*, from 256 to 64 per cell, while leaving the average thermal fluctuation levels in the same range (Figs. 9c and 9d). Furthermore, a numerically stable simulation was performed with $w_h\Delta t_i$ =5.8 and N_*=50 for a smoothing factor a=1.7.

Code timings on a single processor Cray 2 for the semi-implicit orbit-averaged algorithm with fully vectorized gather-scatter [11] for the charge density accumulation and the force interpolation to the particles are displayed in Fig. 10. The timings were calculated by dividing the processing time per electron timestep by the total number of particles ($2N_i$) for equal numbers of electrons and ions. The electron timestep is used so that a reference simulation with equal electron and ion timesteps and equal numbers of particles can be used, against which the code efficiency improvements due to electron subcycling and orbit-averaging can be measured. The reduction in code timing with increasing N_* is a result of the electron subcycling; *i.e.*, we are not advancing the ions as often. The orbit averaging leads to an additional improvement in the total cost of the simulation by allowing the reduction of the number of electrons if $N_*>>1$ while maintaining an acceptable statistical noise level. The timing for advancing an individual electron or ion over its respective timestep remains the same. Thus, we have obtained an order of magnitude improvement in the code timing for a simulation of a warm quiescent plasma through the use of the semi-implicit orbit-averaged algorithm.

4. Concluding Remarks

In this paper, we have reported our experience in implementing a semi-implicit orbit-averaged gyrokinetic particle simulation algorithm. We found that our first algorithm introduced earlier in [2] was subject to a temporally growing error. This motivated the revised algorithm

introduced and analyzed in Sec. 2. Simulation experience with the revised algorithm was reported in Sec. 3. The results of the simulation with the revised algorithm are in substantial agreement with the published results [7] and those from a simulation with an explicit time-integration algorithm for the h_i=4 ITG instability. The simulation results reported in Sec. 3 also demonstrate good electron noise-reduction characteristics and a significant improvement in the code timings for orbit-averaged simulation of a warm quiescent plasma.

The algorithm implementation described here is restricted to the case of a possibly tilted magnetic field with no shear. Some comments on the possible extension of this algorithm to allow for magnetic shear are given in the Appendix. This work should be considered as a stepping stone in the development of more powerful particle simulation methods.

An important limitation on the applicability of the semi-implicit orbit-averaged gyrokinetic algorithm was discovered in the course of our work. The limitation derives from timestep constraints set by the physics of the application. When the dominant timestep constraints are set by accuracy restrictions determined by equilibrium conditions, (*e.g.*, particle Courant conditions set by thermal velocities for the ions and electrons, $v_i\Delta t_i<\Delta x_\parallel$ and $v_e\Delta t_e<\Delta x_\parallel$, where $\Delta x_\parallel=\Delta x/q$, $v_{i,e}^2 = T_{i,e}/m_{i,e}$, and $q=B_y/B_0$ ($<<1$)), then there is a large disparity in timescales: $\Delta t_i/\Delta t_e=O(m_i/m_e)^{1/2}$ for T_i/T_e=O(1). The orbit-averaged algorithm is designed to take advantage of this disparity to achieve an improvement in computational efficiency. Note that because we are specifically interested in physical circumstances for which ion Landau resonance might be important, viz., $w/k_\parallel v_i=O(1)$, the timesteps for the evolution of the fields and the ion advance have been taken to be equal. If most of the electrons are moving much faster than the ions, we need to use a smaller timestep to accurately resolve their trajectories, but we can average their contributions to the charge and current densities in Maxwell's equations to reduce the computational costs. However, the simulation timesteps cannot be chosen without regard to finite-amplitude considerations. In particular, in the gyrokinetic simulation model the electron **E**×**B** velocity V_E and the ion gyroaveraged **E**×**B** V_G must satisfy $V_E\Delta t_e<\Delta x$ and $V_G\Delta t_i<\Delta x$. In general, $V_G \le V_E$, but for $k_\perp \overline{r}_i <<1$, V_G and V_E could be comparable; and there would be little

disparity between the perturbed electron and ion drift velocities. This circumstance presents an impediment to the use of orbit averaging. For example, if $(V_G/v_i)>(\Delta x/\Delta x_{\|})$, then an ion timestep must be used to resolve the perturbed drift motion accurately that is smaller than that determined by resolving the equilibrium thermal streaming parallel to the magnetic field.

In the h_i=4 ITG instability test case reported here, the wave amplitudes and the perturbed drift motion that were observed required the use of a relatively small timestep; and the value of $N_*=\Delta t_i/\Delta t_e$ was relatively small, viz., N_*=3. Relatively large electric potentials were observed: $|e\phi/T_e|\leq 0.18$. The simulation timesteps were constrained by the Courant conditions on the peak velocity perturbations, which satisfied $V_E\Delta t_e/\Delta x=0.3$ and $V_G\Delta t_i/\Delta x=0.08$ for $\Delta t_i/\Delta t_e=3$. With these timesteps, the Courant conditions for the thermal velocities were easily satisfied, $qv_e\Delta t_e/\Delta x=0.06$ and $qv_i\Delta t_i/\Delta x=0.004$ for q=0.01. It should be noted that the simulations with the explicit and semi-implicit algorithms were both subject to these Courant conditions.

Simulations of the ITG instability modeling larger systems with weaker gradients than those used in our examples might be expected to saturate at smaller wave amplitudes and with weaker perturbed drifts on the basis of free energy or mixing-length arguments [7]. Mixing-length arguments lead to estimates for the perturbed electric potential at saturation $e\phi/T_e\sim 1/kL_n$ or $1/kL_t$, where k is the wavenumber appropriate to the fastest growing modes or the modes dominating the fluctuation spectrum. These arguments have been found useful in providing estimates, sometimes upper bounds, for fluid and particle simulations of turbulent transport. Because we know of no better *a priori* estimate of the saturated turbulence, we use the mixing-length estimate to express $V_E/v_e=ck\phi/Bv_e\sim r/L_n$, where r_e is the thermal electron Larmor radius. Thus, V_E/v_e is proprotional to L_n^{-1}; systems with weaker gradients might be more comparatible with the use of large values of Δt_i and N_* in an orbit-averaged algorithm. In general, physics applications in which finite-amplitude effects are relatively weaker so that equilibrium-determined constraints are dominant and in which there is a large disparity between the ion timescales and the faster electron timescales, will provide more fruitful opportunities for the use of the semi-implicit orbit-averaged algorithm.

APPENDIX: Extension of the Algorithm to Include Magnetic Shear

The algorithms described in the text of this paper were restricted to having a tilted, unsheared magnetic field. A more relevant model of the magnetic field for physical applications is one in which there is magnetic shear, $B_y=B_0(x-x_0)/L_s$, where L_s is the magnetic shear length. The methodology of the particle pushing and charge accumulation remains unchanged from the algorithm described in the text, but the solution of the field equation must be revised for magnetic shear. In the presence of magnetic shear, the explicit dependence of $\nabla_\parallel$ on x, $\nabla_\parallel = (\partial/\partial z) + (x - x_0)L_s^{-1}(\partial/\partial y)$, frustrates the use of Fourier transforms in x to solve the semi-implicit Poisson equation, Eq. (4). Here we suggest a method for solving Eq. (4) when there is magnetic shear.

If one cannot Fourier transform in x, then the evaluation of $-(w_{pi}^2/\Omega_i^2)\nabla_\perp^2 g = l_i^{-2}[1 - I_0\exp(-b)]$, where $l_i=v_i/w_i$, cannot be performed in **k** space. Research on gyrofluid models [12] has demonstrated the utility of Padé approximation, $I_0\exp(-b)\approx(1+b^2)^{-1}$ for $0\le b\le 9$. For simplicity we drop the vacuum polarization term ∇^2 in Eq. (3) (which is typically small), use the Padé approximation for $I_0\exp(-b)$, and apply the operator $l_i^2(1+b) = l_i^2(1-\bar{r}_i^2\nabla_\perp^2)$ to both sides of Eq. (3) to obtain

$$\left\{-\bar{r}_i^2\nabla_\perp^2 + l_i^2(1-\bar{r}_i^2\nabla_\perp^2)\nabla\cdot[C_0\mathbf{?}_e\cdot\nabla]\right\}\tilde{f}_{N+1} = l_i^2(1-\bar{r}_i^2\nabla_\perp^2)S. \qquad \text{(A1)}$$

where $S = 4\pi n_e\left(\bar{n}^i_{N+1} - \langle n^e\rangle_{N+1} - \nabla\cdot[C_0\mathbf{?}_e\cdot\nabla f_N]\right)$ has explicit dependence on x through $\nabla_\parallel$ (see Eq. (4)). The expression in the curly bracket on the left side of Eq. (A1) is an elliptic operator whose finite-difference representation in x leads to a matrix that is sparse and banded. Fourier transforms can still be used to evaluate the y and z derivatives in **k** space. We expect that the solution of the resulting sparse-matrix equation will be amenable to one of the many methods

that exist for such equations, but we have made no attempt to implement this algorithm extension as yet.

Acknowledgments

We are grateful to J. Byers, A. Dimits, L. LoDestro, and R. Sydora for their useful comments and providing a critical audience during the course of our research. This work was performed by the Lawrence Livermore National Laboratory under the auspices of the United States Department of Energy under Contract W-7405-Eng-48.

References

1. B. I. Cohen, in *Multiple Time Scales*, edited by J. U. Brackbill and B. I. Cohen (Academic Press, Orlando, FL, 1985), p. 311.
2. B. I. Cohen and T. J. Williams, *J. Comput. Phys.* 97, 224 (1991).
3. W. W. Lee, *J. Comput. Phys.* 72, 243 (1987).
4. A. Friedman, A.B. Langdon, and B. I. Cohen, *Comments Plasma Phys. Controlled Fusion* 6, 225 (1981).
5. B. I. Cohen, T. A. Brengle, D. B. Conley, and R. P. Freis, *J. Comput. Phys.* 38, 45 (1980).
6. B. I. Cohen, R. P. Freis, and V. A. Thomas, *J. Comput. Phys.* 45, 345 (1982).
7. W. W. Lee and W. M. Tang, *Phys. Fluids* 31, 612 (1988).
8. A. B. Langdon, B. I. Cohen, and A. Friedman, *J. Comput. Phys.* 51, 107 (1983).
9. B. I. Cohen, A. B. Langdon, and A. Friedman, *J. Comput. Phys.* 56, 51 (1984).
10. J. C. Adam, A. Gourdin-Serveniere, and A. B. Langdon, *J. Comput Phys.* 47, 229 (1982).
11. A. Heron and J. C. Adam, *J. Comput. Phys.* 85, 284 (1989).
12. G. W. Hammet, W. Dorland, and F. W. Perkins, *Phys. Fluids B* **4**, 2052 (1992).

Figures

Figure 1

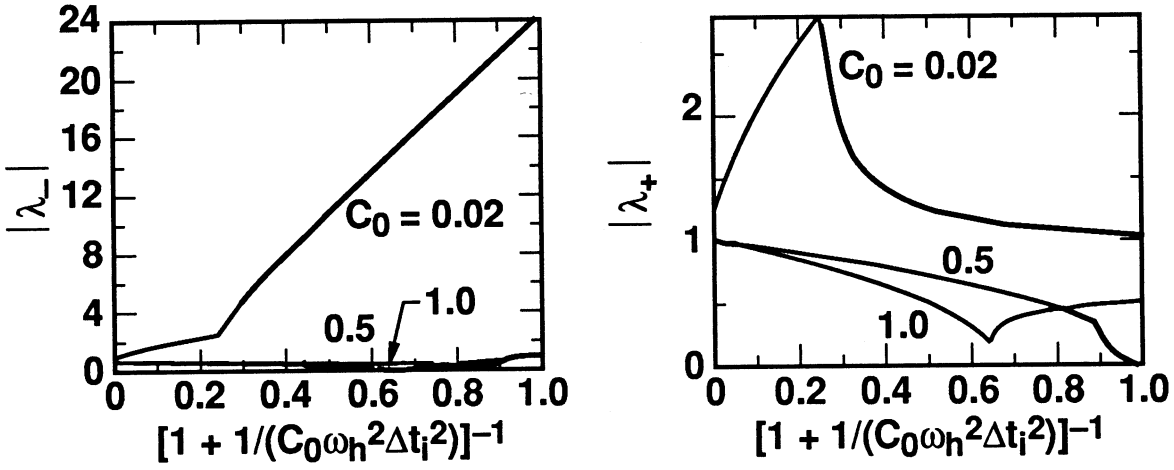

Fig. 1. The modulus of the amplification factor $|\lambda|$ as function of $w_h^2 \Delta t_i^2$ for C_0=0.02, 0.5, 1.0 in the first algorithm.

Figure 2

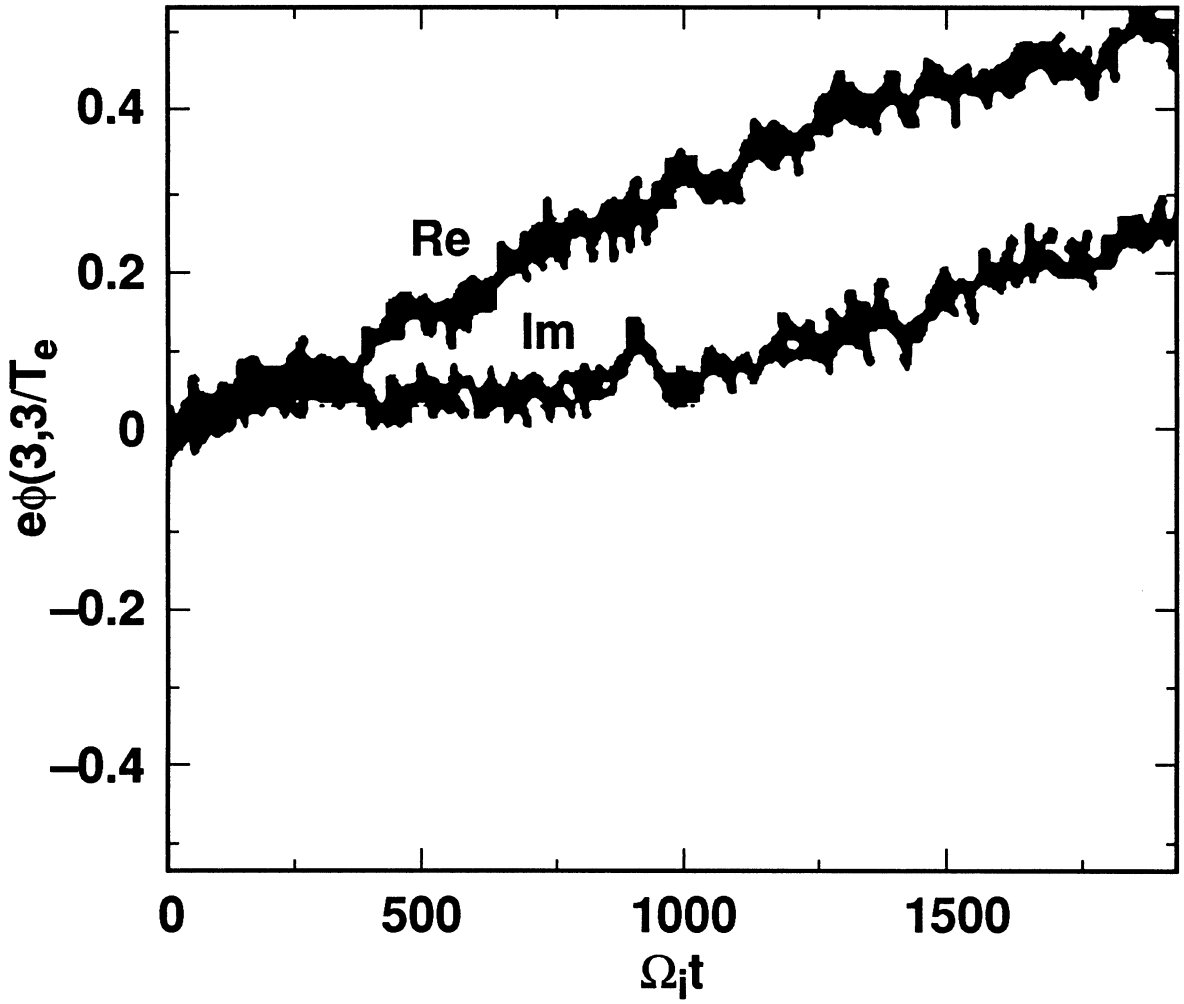

Fig. 2. The real and imaginary parts of the (k_x,k_y)=(3,3) Fourier component of ef/T_e as a function of time.

Figure 3

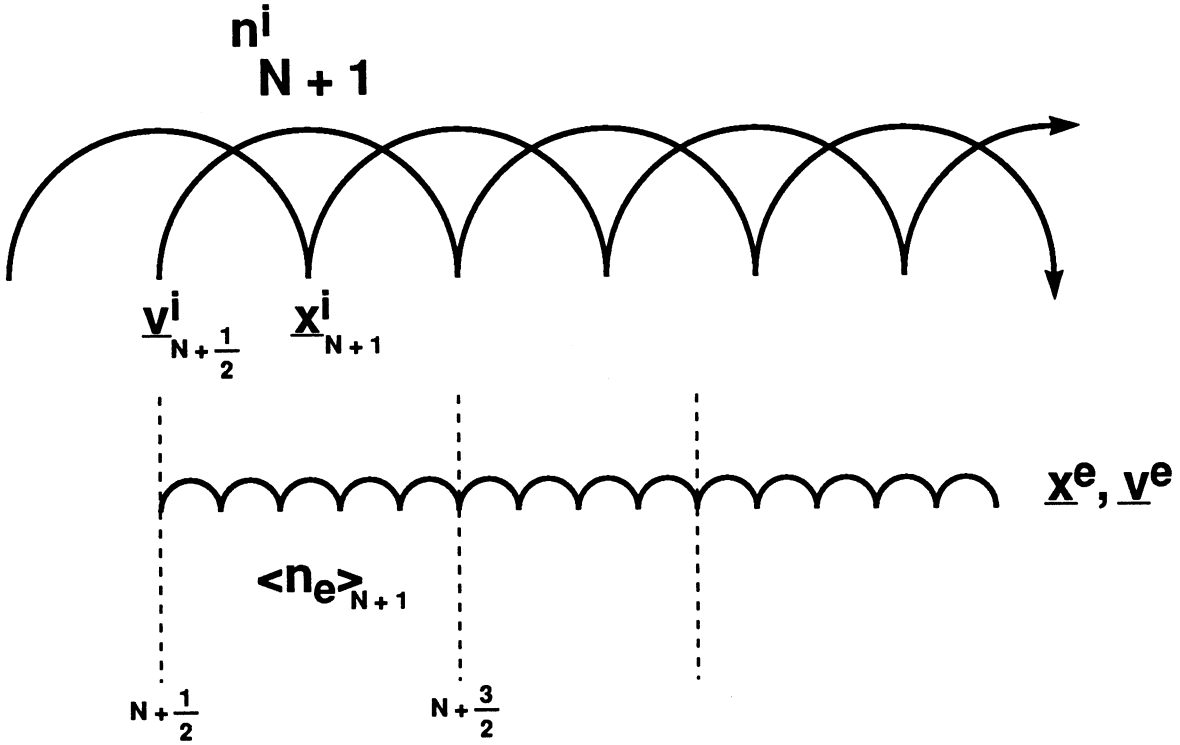

Fig. 3. Interleaving of advancing ions and electrons, and solving for the self-consistent electric field in the revised orbit-averaged algorithm.

Figure 4

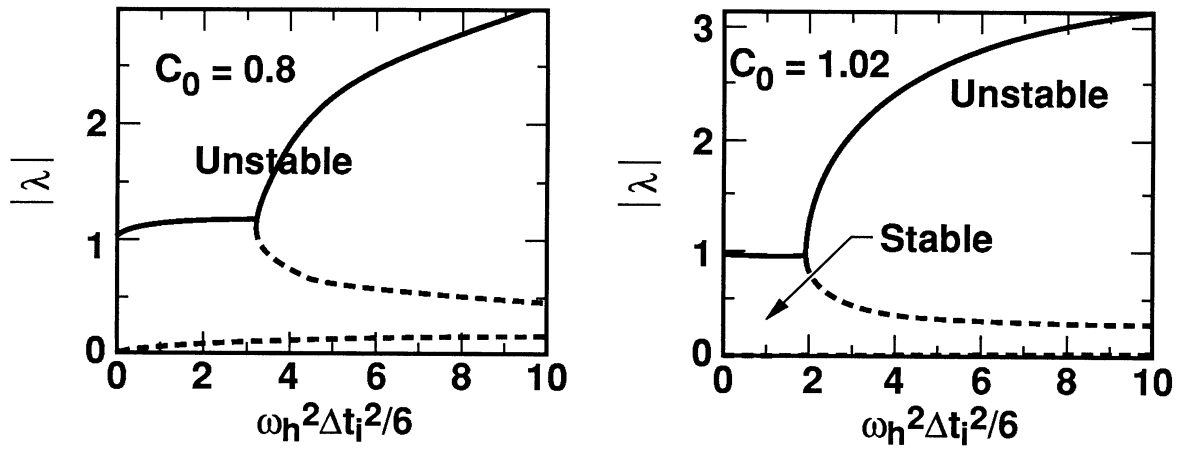

Fig. 4. The modulus of the amplification factor |λ| as a function of $w_h^2 \Delta t_i^2 / 6$ for C_0=0.8 and 1.02 in the revised algorithm.

Figure 5

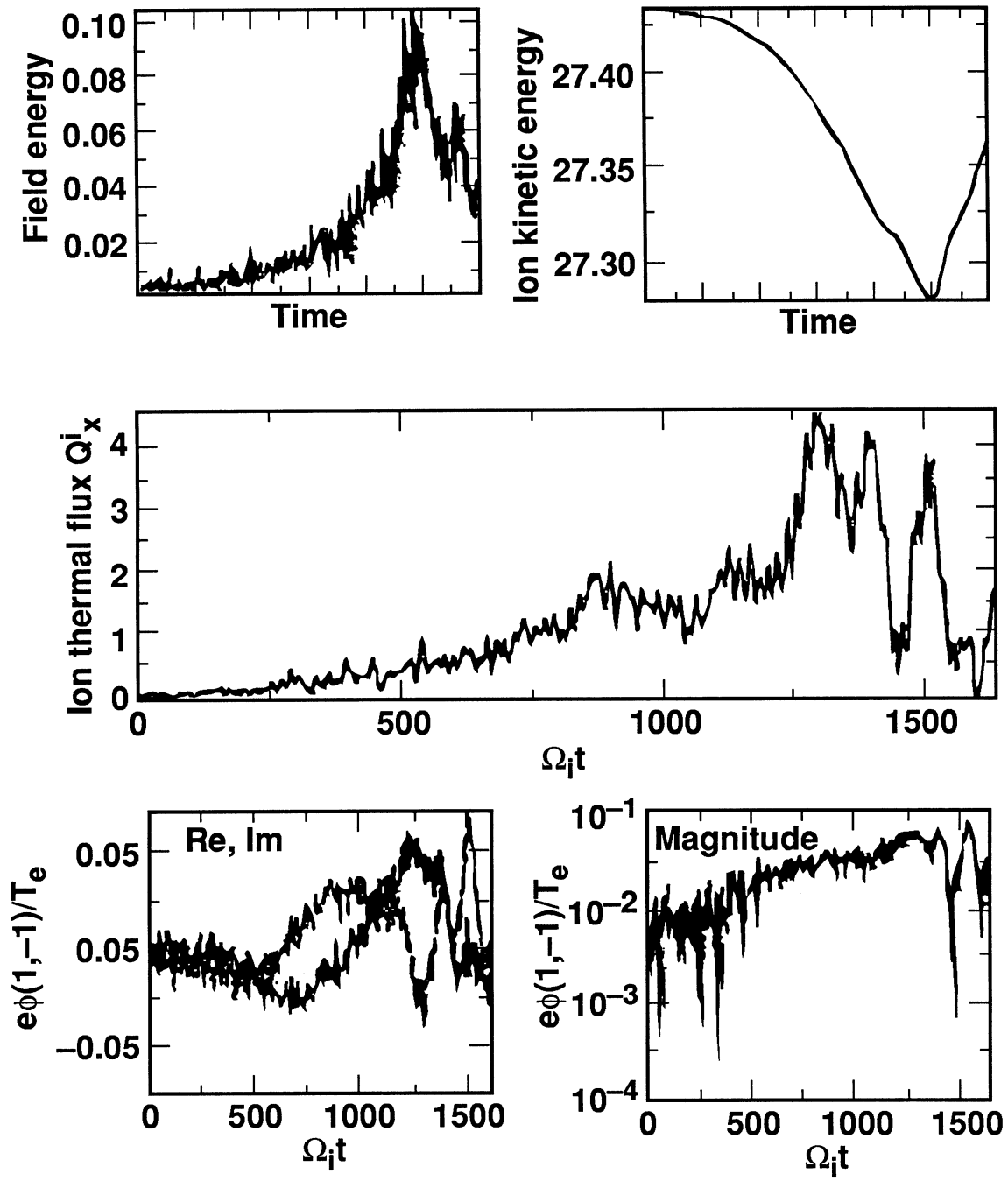

Fig. 5. Simulation results from an explicit subcycled simulation of the h_i=4 instability in an unsheared magnetic field. The thermal ion flux has been summed over all the ions and normalized to the product of the number of ions times the ion temperature and the ion sound speed. The ion kinetic energy is the sum of all the ion kinetic energies in code units, and the field energy is the sum of the electric field and the ion polarization dielectric energy densities integrated over the volume in the same units as the ion kinetic energy. It is the nature of the ITG instability that the ion parallel kinetic energy is depleted at the expense of exciting the ITG modes to finite amplitudes. The real and imaginary parts and the magnitude of the Fourier amplitude of $|ef/T_e|$ for the (k_x, k_y)=(1,−1) mode are also plotted as a function of time.

Figure 6

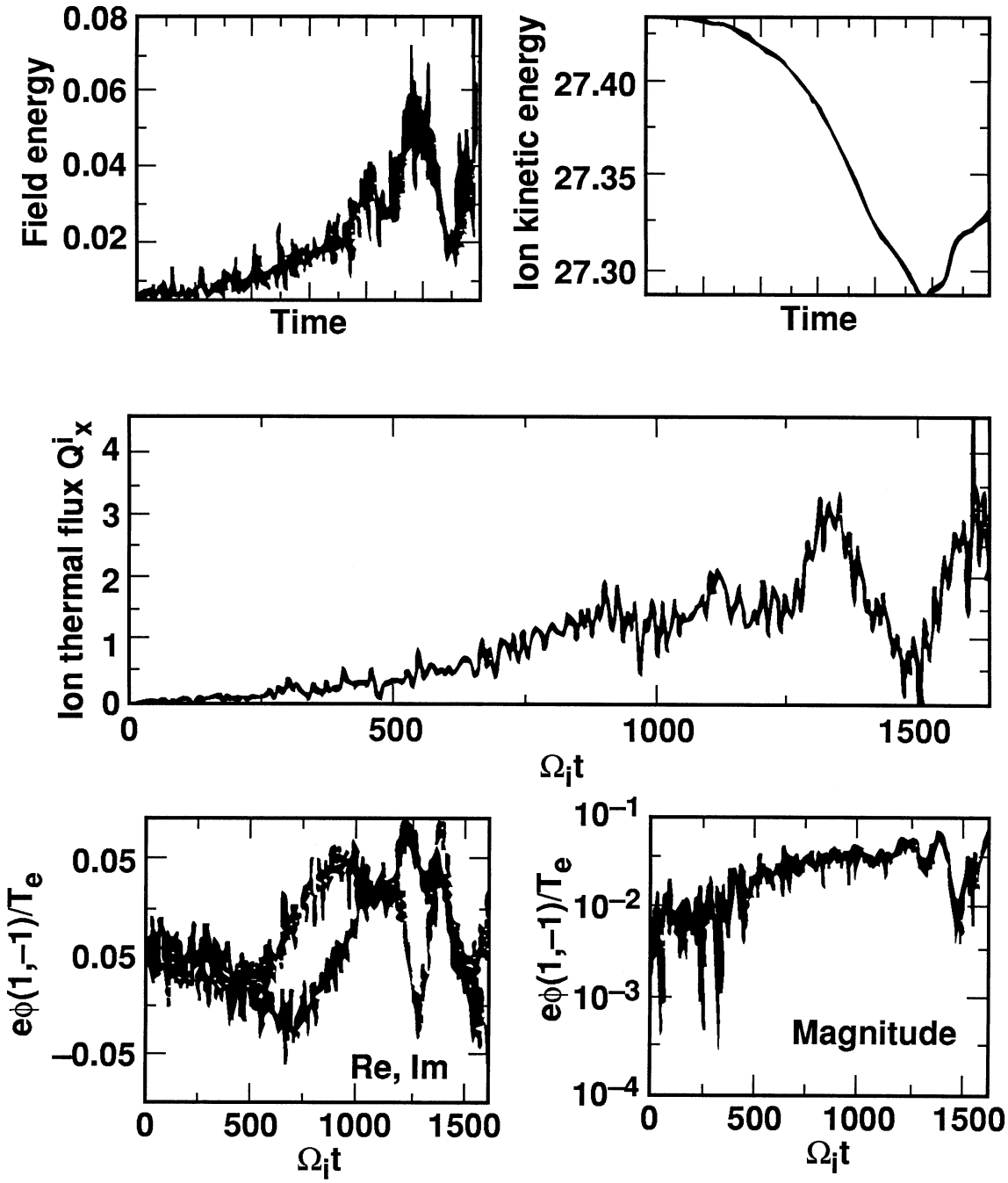

Fig. 6. Simulation results from a semi-implicit orbit-averaged simulation of the h_i=4 instability with equal numbers of electrons and ions.

Figure 7

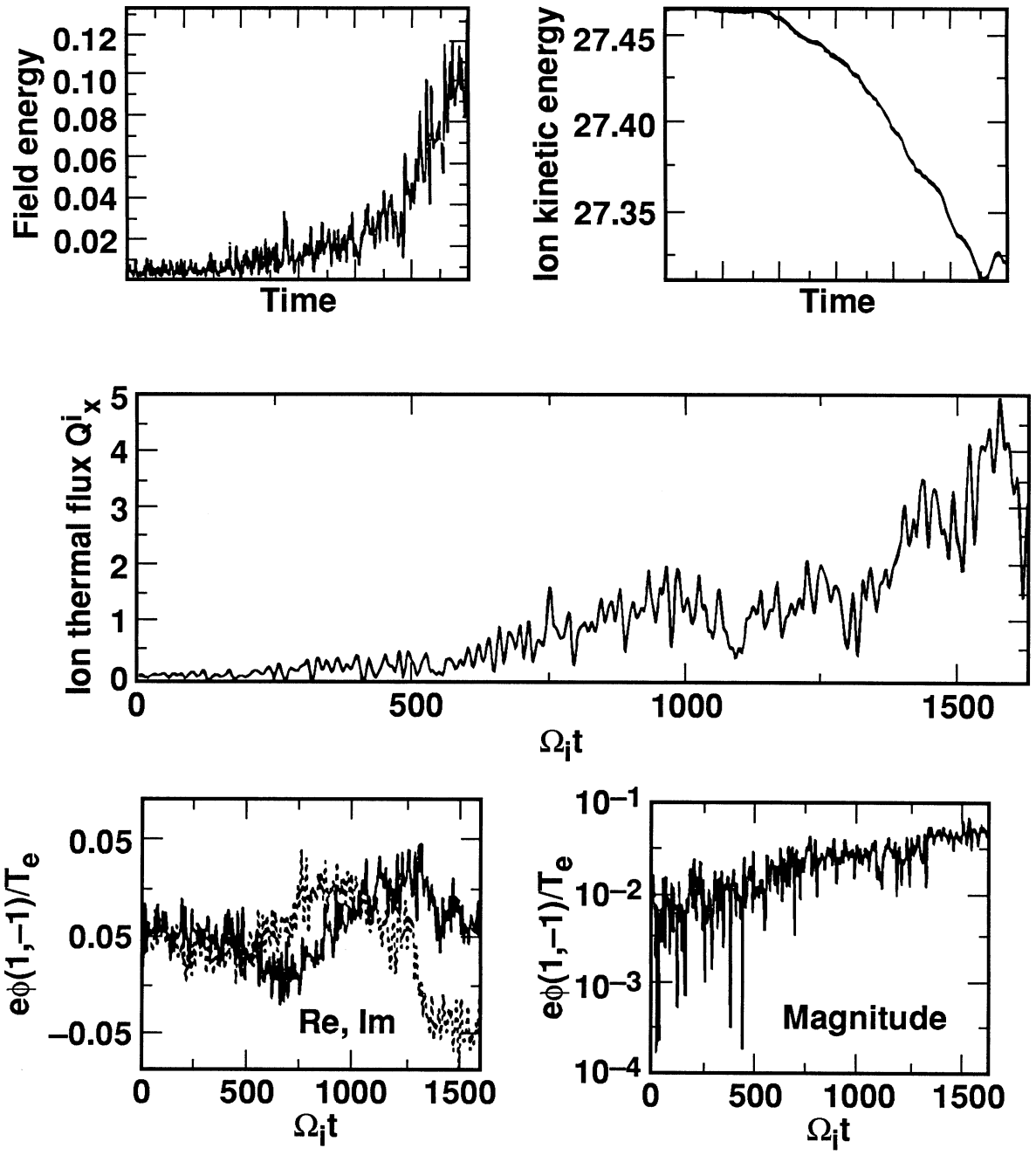

Fig. 7. Simulation results from a semi-implicit orbit-averaged simulation of the h_i=4 instability with half as many doubly-charged electrons as ions.

Figure 8

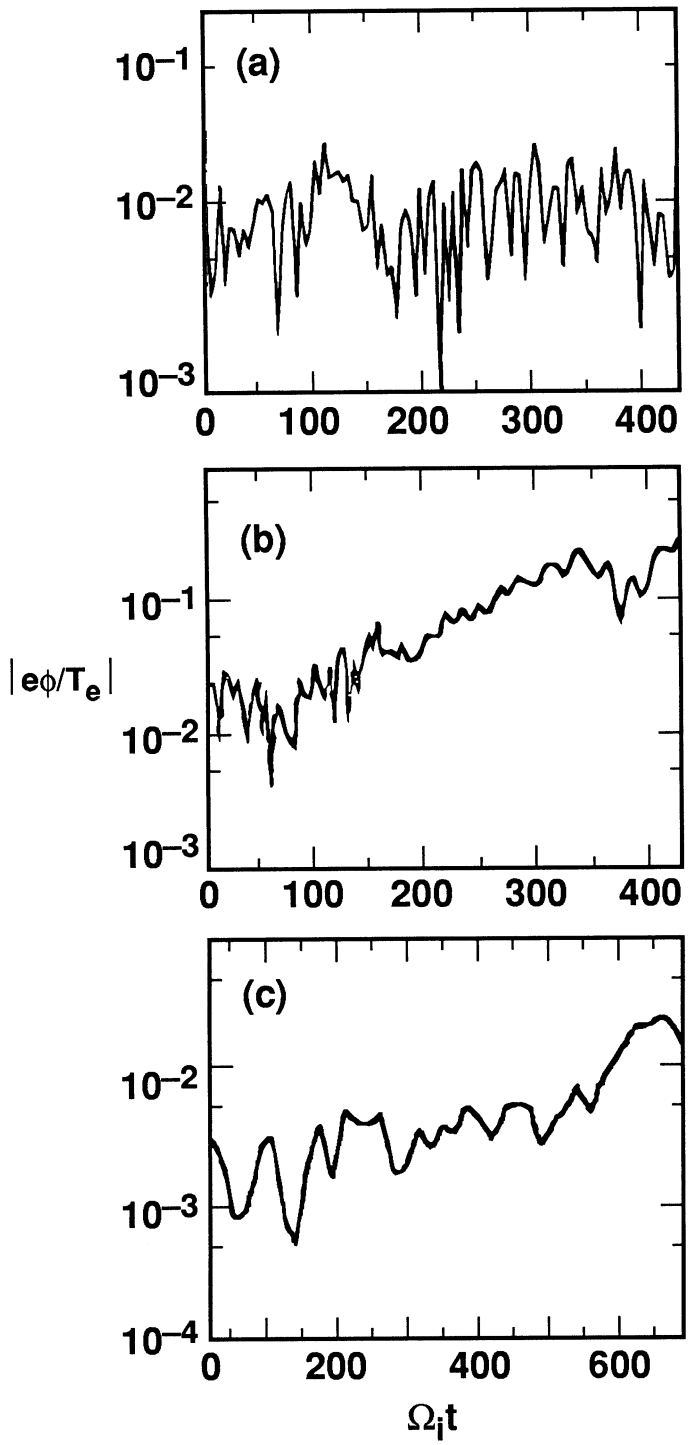

Fig. 8. Plots of $|ef/T_e|$ for the $(k_x, k_y)=(1,-1)$ Fourer mode from semi-implicit orbit-averaged simulations of a warm quiescent plasma for (a) $C_0=1.04$ and $w_h\Delta t_i=1.86$, (b) $C_0=0.5$ and $w_h\Delta t_i=1.86$, and (c) $C_0=1.04$ and $w_h\Delta t_i=7.4$.

Figure 9

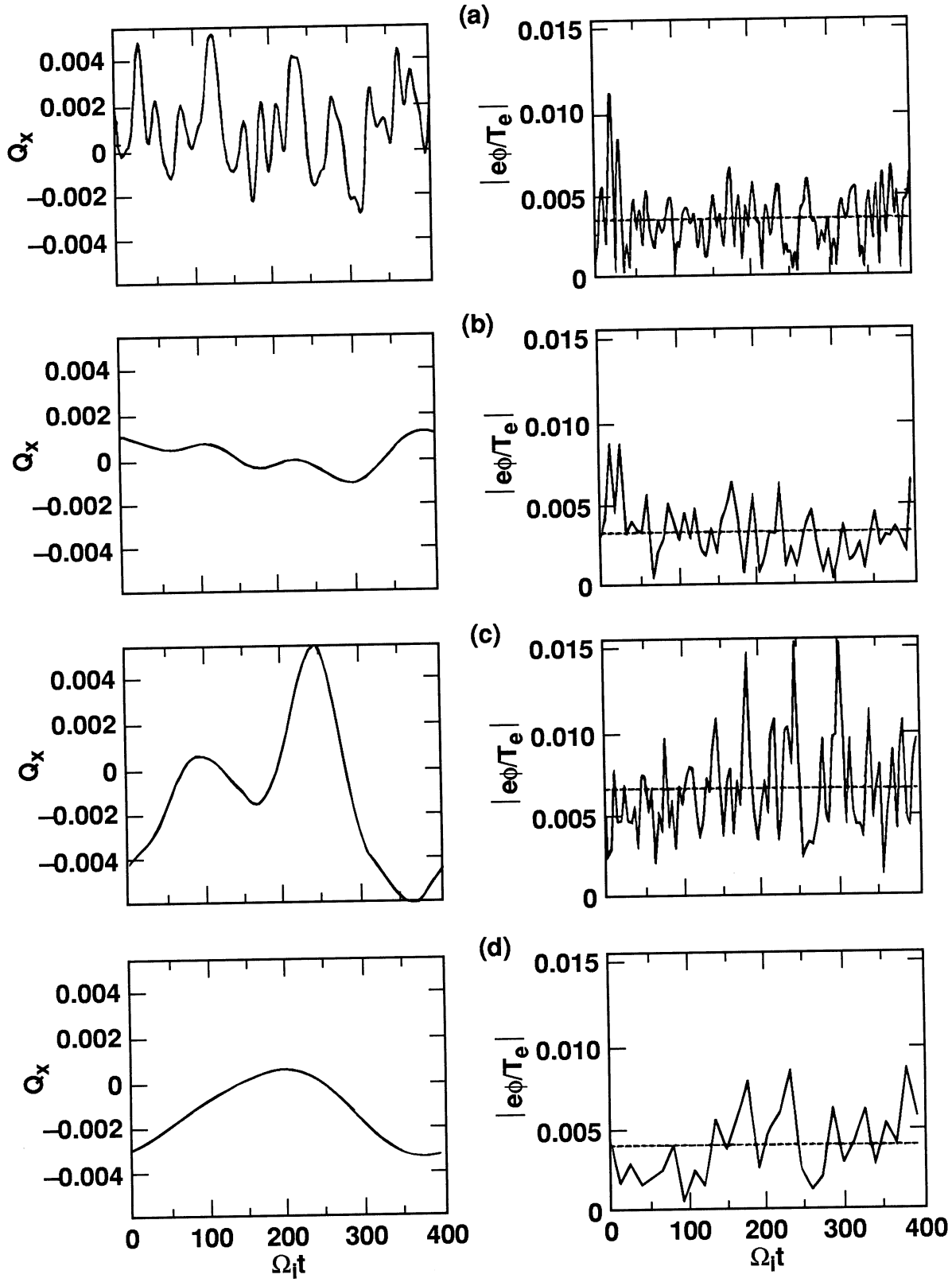

Fig. 9. Simulation results for the normalized, time-filtered ion thermal flux Q_x in x *and* $|ef/T_e|$ for the $(k_x,k_y)=(1,-1)$ Fourier mode as functions of time for a warm quiescent plasma. (a) 256 electrons per cell, $N_*=3$, and the explicit subcycled algorithm. (b) 256 electrons per cell, $N_*=25$, and the semi-implicit orbit-averaged algorithm. (c) 64 electrons per cell, $N_*=16$, and the semi-implicit orbit-averaged algorithm. (d) 64 electrons per cell, $N_*=50$, and the semi-implicit orbit-averaged algorithm. The dashed curves on the $|ef/T_e|$ plots have been time-filtered.

Figure 10

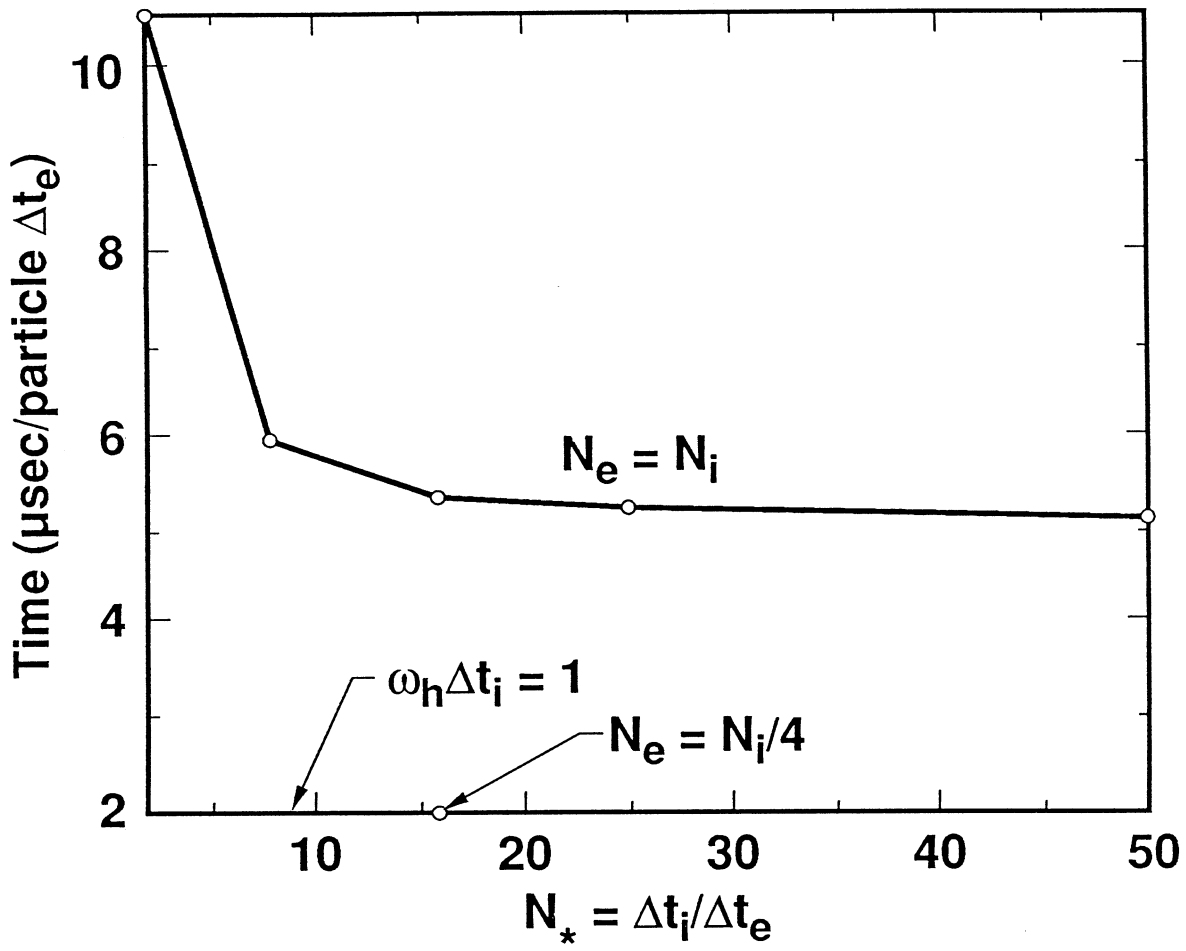

Fig. 10. Code timings (per particle per timestep) for semi-implicit orbit-averaged simulations of a warm quiescent plasma as a function of the subcycling parameter $N_*=\Delta t_i/\Delta t_e$ for equivalent numbers of ions and electrons, and for one-fourth the number of electrons in a simulation that obtained similar physical results.